



# Multimodal dispersive waves in a free rail: Numerical modeling and experimental investigation

Pan Zhang, Shaoguang Li, Alfredo Núñez, Zili Li \*

Delft University of Technology, Section of Railway Engineering, Stevinweg 1, 2628 CN Delft, the Netherlands



## ARTICLE INFO

### Article history:

Received 11 January 2020

Received in revised form 4 September 2020

Accepted 12 September 2020

Available online 29 September 2020

### Keywords:

Multimodal dispersive waves

Phase and group velocities

Operating deflection shapes

Synchronized multiple-acceleration wavelet

## ABSTRACT

In this paper, we present a solution method based on finite element (FE) modeling to predict multimodal dispersive waves in a free rail. As well as the modal behaviors and wavenumber-frequency dispersion relations, the phase and group velocities of six types of propagative waves are also derived and discussed in detail in the frequency range of 0–5 kHz. To experimentally distinguish different types of wave modes, the operating deflection shape (ODS) measurement approach is employed in the laboratory. ODS is measured from the spatial distribution of imaginary parts of the FRFs. We also propose a synchronized multiple-acceleration wavelet (SMAW) approach to experimentally study the propagation and dispersion characteristics of waves in a free rail. The group velocities in the vertical, longitudinal and lateral directions are estimated from the wavelet power spectra (WPSs). The good agreement between the simulation and measurement in terms of mode shapes and ODSs, wavenumber-frequency dispersion curves, and group velocities indicates that the ODS and SMAW approaches are capable of distinguishing different wave modes and measuring wave propagation and dispersion characteristics. In situ experimental results further demonstrate the effectiveness of the ODS measurement for coupled modal identification and the SMAW approach for wave dispersion analysis of the rail in a field track.

© 2020 The Authors. Published by Elsevier Ltd. This is an open access article under the CC BY license (<http://creativecommons.org/licenses/by/4.0/>).

## 1. Introduction

Rail vibrations play an important role in wheel-rail interactions, especially in the high-frequency range. Noise and corrugation problems in railway engineering are related to rail vibrations; for example, the lateral and vertical rail modes dominate rolling noise radiation from 500 to 1600 Hz and generally remain important at higher frequencies up to 5 kHz [1]. Short pitch corrugation has been reported to be related to the ‘pinned-pinned’ resonance at approximately 1 kHz [2,3], which is a rail vertical bending mode with a wavelength of two sleeper spacings. Recently, new insights into short pitch corrugation have proposed that longitudinal rail modes are responsible for corrugation initiation [4]. Therefore, investigations of rail vibrations in the vertical, longitudinal and lateral directions are of great importance for understanding these problems.

Rail vibrations can be seen as the superposition of a series of propagative waves [1]. Wavenumber-frequency dispersion relations, and phase and group velocities provide fundamental information to understand wave propagation characteristics. In the literature, many models have been developed to model the rail, including analytical beam or plate models [5–11,14], the semi-analytical or 2.5D FE model (SAFE) [12,15,18–20], and the 3D FE model [11,13,17]. The analytical beam or plate

\* Corresponding author.

E-mail address: [Z.Li@tudelft.nl](mailto:Z.Li@tudelft.nl) (Z. Li).

models assume a constant cross-section of the rail, which is only valid at low frequencies [9]. The 2.5D FE model and 3D FE model can both consider rail cross-section deformation, which is important to accurately predict the dispersion relations. Although the computation efficiency of the 2.5D FE model is higher because it treats the longitudinal direction analytically, the 3D FE model has the advantages that it is capable of modeling nonlinear wheel-rail dynamic contact, which is important when studying wheel-rail rolling noise and short pitch corrugation. Many papers [16,18–21] have reported on the dispersion curves and phase and group velocities of rail waves in the ultrasound frequency range (i.e., 100 kHz) for long-range rail inspection. In the frequency range of rolling noise and short pitch corrugation (below 5 kHz), Thompson [9] and Gavric [12] predicted the dispersion curves, while the phase and group velocities were not presented. In this paper, we applied a 3D FE model to predict the dispersive waves in a free rail at 0–5 kHz and derived the phase and group velocities.

Although many models have predicted the multiple wave modes in a free rail [9,12,16], few experimental methods have been reported in the literature to distinguish different wave modes. One possible reason is that most researchers have focused only on the vertical rail vibration because the wheel-rail excitation mainly acts in this direction [5,10,13]. There is only one type of wave mode called the vertical bending mode in this direction; thus, the influence of modal coupling is insignificant. However, when studying three-dimensional rail vibrations, modal coupling of different directions may occur, which makes one natural frequency correspond to multiple rail modes. In this case, the widely used experimental method for the railway structure, frequency response function (FRF) measurement [22–24], has difficulty identifying the coupled modes because it can only obtain the natural frequencies. Another experimental method named operating deflection shape (ODS) measurement can derive both the natural frequencies and the corresponding mode shapes. In the literature [25–28], this method has been successfully applied in specific engineering structures such as beams and plates. The modes were uncoupled in these studies because the beams and plates have relatively simple cross-sections, and the research interest only focused on the vertical direction at frequencies lower than 1600 Hz. In this work, the rail has a more complicated arbitrary cross-section geometry, and our research interest is three-dimensional rail vibrations up to 5 kHz. Considerably more vibration modes (hundreds) need to be dealt with, and they may couple with each other. Coupled modes have dissimilar wavelengths that hinder the ability of sensors to capture them simultaneously. In this paper, the ODS measurement will be used to distinguish coupled wave modes in a free rail.

In addition to the multiple modes, dispersion is another feature of the propagative waves in a rail that makes the experimental identification of waves more difficult [9,12,16]. For the experimental analysis of the propagation and dispersion of elastic waves, the wavelet transform (WT) has been proven to be an effective tool [18,29–33]. Lanza [34] applied this time-frequency analysis method in railway tracks and obtained group velocity dispersion curves for the vertical, longitudinal, and lateral rail vibration modes at 1–7 kHz. Only qualitative agreement was achieved with Gavric's numerical simulation results [12]. The deviations between the measurement and simulation may have been caused by the different boundary conditions of the rail. In Gavric's simulation, the rail had a free-free boundary, while in Lanza's experiment, the rail was supported by steel pads on wooden sleepers, which introduced additional stiffness and damping to the rail. In addition, the accuracy of the single-acceleration wavelet approach used in Lanza's experiment might have been reduced by the wave reflection at the rail ends. To improve the experimental accuracy and achieve better agreement with the simulation, a synchronized multiple-acceleration wavelet (SMAW) approach will be developed in this paper. The test boundary condition will also be improved by the experimental setup to better match the free-free boundary of the FE simulation.

The purpose of this work is to gain a better understanding of free rail vibrations and provide experimental methods to distinguish different wave modes and measure wave propagation and dispersion characteristics. The paper is organized as follows. In Section 2, a 3D FE model is built to predict the multimodal dispersive waves in a free rail. The modal behavior, wavenumber-frequency dispersion relations, and phase and group velocities of these waves are derived. In Section 3, two methods—ODS measurement and SMAW measurement—are introduced for the experimental investigation of the multimodal dispersive waves. In Section 4, the experimental results, including ODSs, wavenumber-frequency dispersion curves, WPSs and group velocities, are obtained and compared with the simulations. Section 5 discusses the advantages and disadvantages of ODS measurements and SMAW measurements and the effectiveness of these two methods in field tracks. The main conclusions are drawn in Section 6.

## 2. Numerical simulation of multimodal dispersive waves in free rail

In this section, we present a solution method based on FE modeling to predict the multimodal dispersive waves in a free rail. The method includes 1) building a 3D FE model of a free rail using ANSYS; 2) a modal analysis to derive the natural frequencies, modal shapes, and cross-section deformation; and 3) a numerical prediction of dispersion relations by postprocessing the modal results, including phase and group velocities. Fig. 1 shows a flowchart of this method.

### 2.1. 3D FE model

A 3D FE rail model is built with ANSYS, as shown in Fig. 2a. The rail is modeled with 8-node solid elements based on the measured UIC 54E1 profile used in the experimental setup in Section 4. The rail length in the model is 4.97 m. Fig. 2b shows the mesh of the rail cross-section. The rail profile is discretized with an equal element edge length of 4 mm. The longitudinal element size is 10 mm. As the mesh size, model length and rail profile are crucial parameters for FE prediction, their details

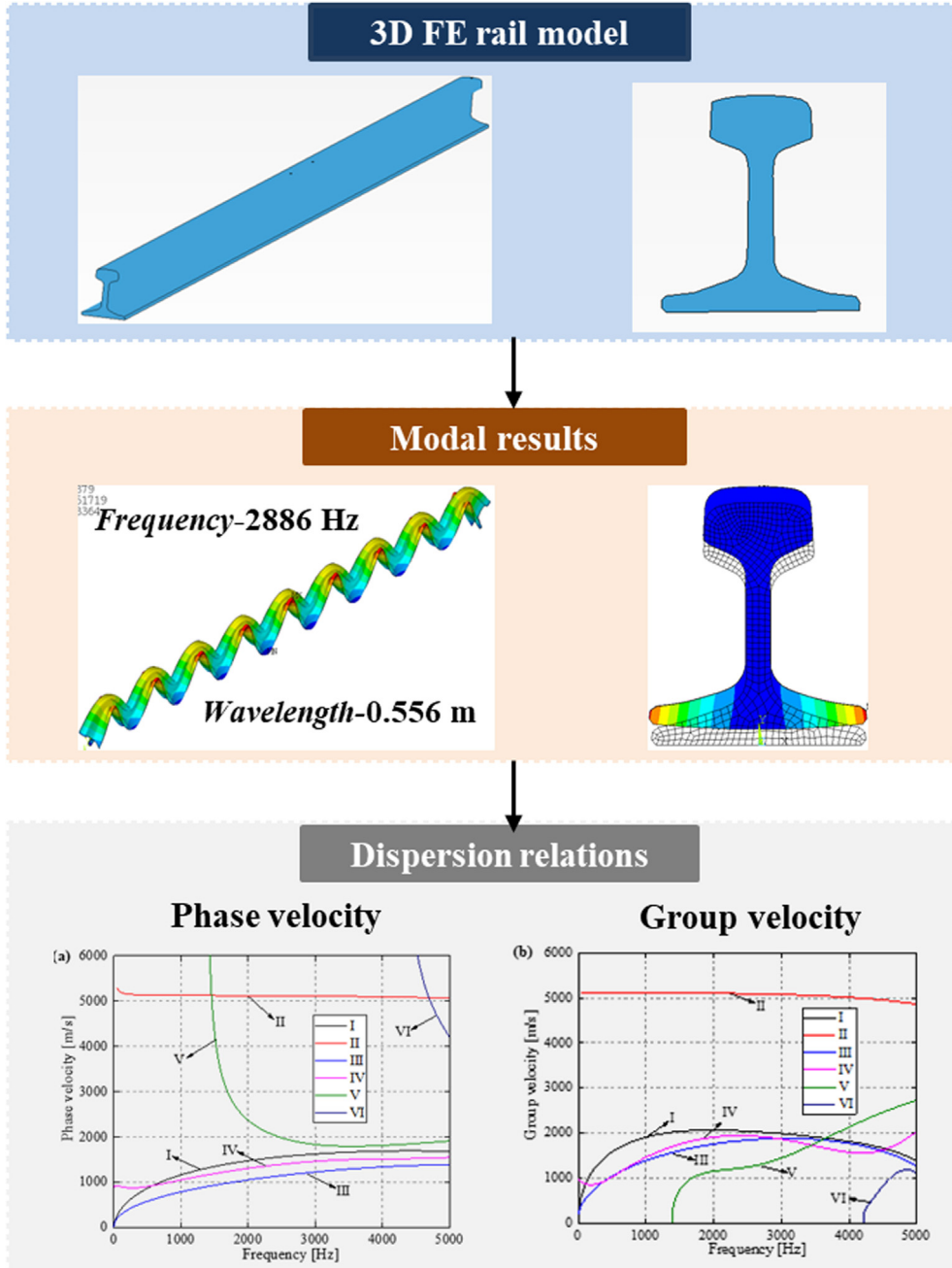


**Fig. 1.** Flowchart of the solution method based on FE modeling.

are discussed in the Appendix. The rail material is treated as elastic and isotropic with a Young's modulus of 210 GPa, a Poisson's ratio of 0.3 and a density of  $7850 \text{ kg/m}^3$ . A free boundary condition is applied, and no damping effect is considered. The dynamic behaviors of the rail are studied through modal analysis. The mode extraction method used is Block Lanczos, and the analyzed frequency range is up to 5 kHz.

## 2.2. Modal results

Six types of characteristic modes of the rail are extracted in the vertical, longitudinal, and lateral directions up to 5 kHz. The modes in the vertical and longitudinal directions are specifically referred to as vertical bending modes (designated 'I' in Fig. 3) and longitudinal compression modes (II). The modes in the lateral direction include four types of cross-sectional

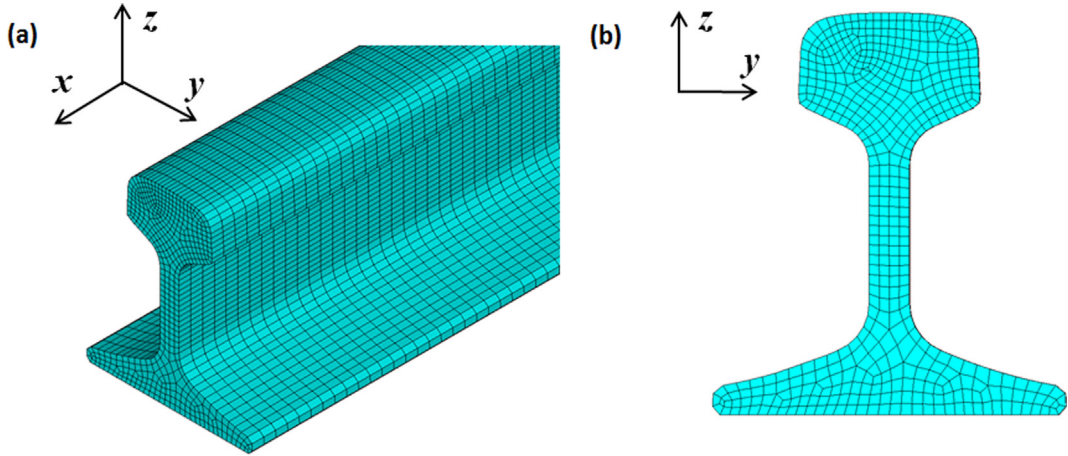


**Fig. 2.** 3D FE rail model: (a) overview of rail model; (b) mesh of cross-section.

deformation, regarded as lateral bending modes (III), lateral torsion modes (IV), web 1<sup>st</sup> bending modes (V), and web 2<sup>nd</sup> bending modes (VI). Each mode is described in terms of three features: modal frequency, mode shape and cross-sectional deformation.

For all six types of modes, the modal shapes in the longitudinal direction (**x** direction) are approximately sinusoidal, and their wavelengths ( $\lambda$ ) are derived from the FE simulation. The wavelengths of vertical bending modes (I) and lateral bending modes (II) are approximately  $2L/(N + 0.5)$ , and wavelengths of the other four types of rail modes are approximately  $2L/N$ , where  $L$  is the rail length, and  $N$  is an integer.

Fig. 3 shows the cross-sectional deformation of the six types of rail modes. The color contrast indicates the relative displacements of the elements. Blue is the minimum displacement, and red is the maximum.

For vertical bending modes (I), the rail moves vertically and has no cross-sectional deformation below around 1 kHz, at which point the rail foot begins to flap. At higher frequencies, rail foot flapping becomes increasingly dominant, while the displacement of the rail head decreases. For longitudinal compression modes (II), the rail has dominant axial displacement, and the cross-section does not deform in the whole frequency range of 0–5 kHz.

With lateral bending modes (III), the rail undergoes lateral displacement and exhibits no cross-sectional deformation below around 420 Hz, at which point the rail foot starts rotating. As the frequency increases, the rail head displacement decreases and rail foot rotation increases, which causes the deformation of the rail web. Above around 4600 Hz, the rail head is almost stationary, and rail foot rotation dominates the rail vibration. For lateral torsion modes (IV), the rail movement can be seen as a rigid rotation of the cross-section at low frequency. As the frequency increases, the rotation of the rail head decreases and is replaced by horizontal displacement, while the deformation shape of the rail foot remains almost unchanged, which together results in rail web bending.

Web 1<sup>st</sup> bending modes (V) start from 1570 Hz. For these modes, the rail head rotates out of phase with the rail foot and causes significant bending of the rail web. The largest deformation of the rail web occurs near its middle part. Web 2<sup>nd</sup> bending modes (VI) appear first at around 4400 Hz. In contrast to web 1<sup>st</sup> bending modes, the rail head rotates in phase with the rail foot for these modes and results in double bending of the rail web. The largest deformation of the rail web occurs at its two ends, and the middle part is nearly stationary.

### 2.3. Dispersion relations

The characteristic modes outlined above (standing waves) are directly equivalent propagative waves of an infinite rail [9]. Each natural frequency and wavelength corresponds to a point on the wavenumber-frequency dispersion curves. The wavenumbers are calculated by  $k = 2\pi/\lambda$ , where  $\lambda$  is the wavelength,  $k$  is the wavenumber.

Fig. 4 shows the dispersion curves of the six types of waves by connecting the discrete wavenumber-frequency points in a frequency range of 0–5 kHz. These waves are distinguished with different symbols and Roman numerals. Vertical bending waves (I), longitudinal compression waves (II), lateral bending waves (III) and lateral torsion waves (IV) all cut on at 0 Hz. Web 1<sup>st</sup> and 2<sup>nd</sup> bending waves (V, VI) propagate from 1570 Hz and 4440 Hz, respectively. Longitudinal compression waves (II) have the largest curve gradients, while web 2<sup>nd</sup> bending waves (VI) have the smallest gradients. Vertical bending waves (I) and lateral torsion waves (IV) cross each other at approximately 660 Hz, which indicates that these two waves may exhibit mode coupling and swap their modal shapes at this frequency. Similar phenomena occur for longitudinal compression waves (II) and web 1<sup>st</sup> (V) and 2<sup>nd</sup> bending waves (VI) at 1640 Hz and 4800 Hz, respectively. When the rail is symmetrical, this mode coupling and veering between different waves are negligible [17].

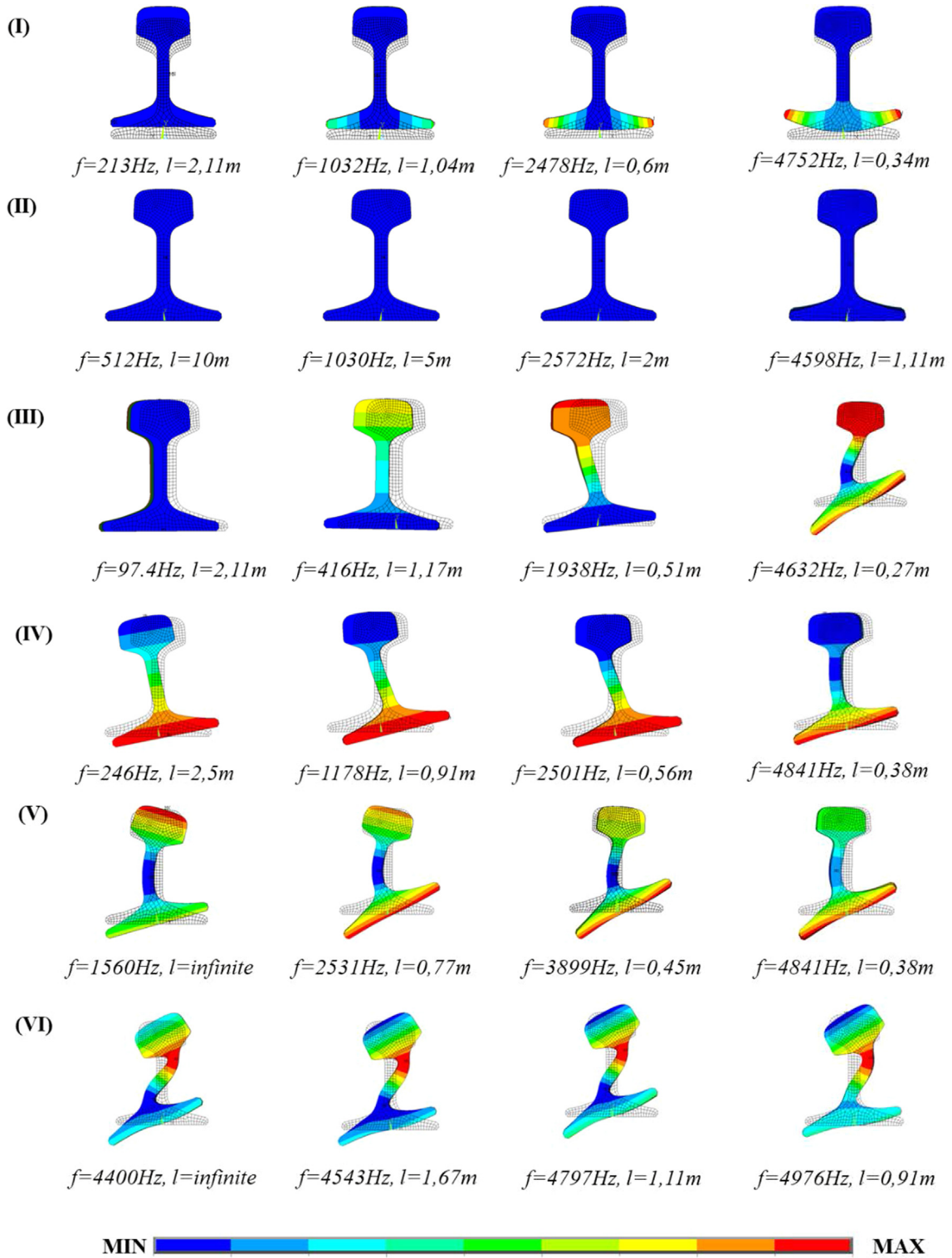


**Fig. 3.** Cross-sectional deformation of vertical bending modes (I), longitudinal compression modes (II), lateral bending modes (III), lateral torsion modes (IV), web 1<sup>st</sup> bending modes (V), and web 2<sup>nd</sup> bending modes (VI).

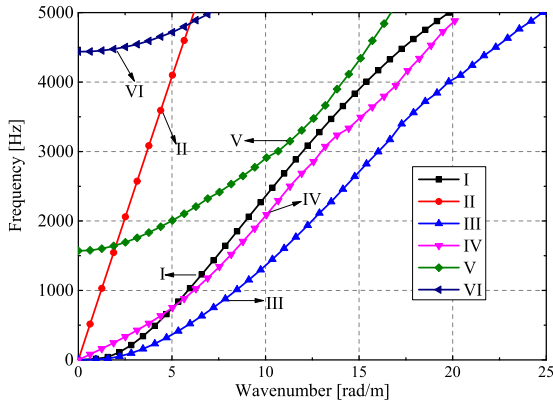


**Fig. 4.** Wavenumber-frequency dispersion curves of vertical bending waves (I), longitudinal compression waves (II), lateral bending waves (III), lateral torsion waves (IV), web 1<sup>st</sup> bending waves (V), and web 2<sup>nd</sup> bending waves (VI).

The results of Fig. 3 and Fig. 4 are in agreement with those in [9,12]. The small differences, such as ‘cut-on’ frequencies of web 1<sup>st</sup> and 2<sup>nd</sup> bending waves are likely to be caused by the different rail profiles (BR flat-bottomed rail in [9] and UIC861-3 in [12]) used for the prediction.

Two kinds of wave velocities, phase and group velocities, are typically used to describe wave propagation characteristics in two aspects. They are calculated from the wavenumber-frequency relation as follows [35]:

$$v_p = \frac{\omega}{k} = 2\pi \frac{f}{k} \quad (1)$$

$$v_g = \frac{d\omega}{dk} = 2\pi \frac{df}{dk} \quad (2)$$

where  $v_p$  is the phase velocity,  $v_g$  is the group velocity,  $\omega$  is the angular frequency,  $f$  is the ordinary frequency and  $k$  is the wavenumber. From (1) and (2), it can be seen that the phase velocity is the secant slope at a point on the wavenumber-frequency curve multiplied by  $2\pi$ , and the group velocity is the corresponding tangential slope multiplied by  $2\pi$ .

Fig. 5 shows the derived phase and group velocity dispersion curves. Vertical bending waves (I) are dispersive waves since the velocities are frequency-dependent. The phase velocity of this type of wave starts from 0 m/s at the cut-on frequency, then increases gradually to approximately 1670 m/s at 3.6 kHz, and remains almost constant at higher frequencies. The group velocity also starts from 0 m/s at 0 Hz and then rises dramatically but with a decreasing rate to approximately 2000 m/s at 1 kHz. At 1–3 kHz, it is approximately frequency-independent, and at higher frequencies, a slight decrease appears.

Longitudinal compression waves (II) can be regarded as nondispersive waves in a frequency range of 0–5 kHz, although a gradually decreasing trend is found for both the phase and group velocity as the frequency increases. The average velocity of

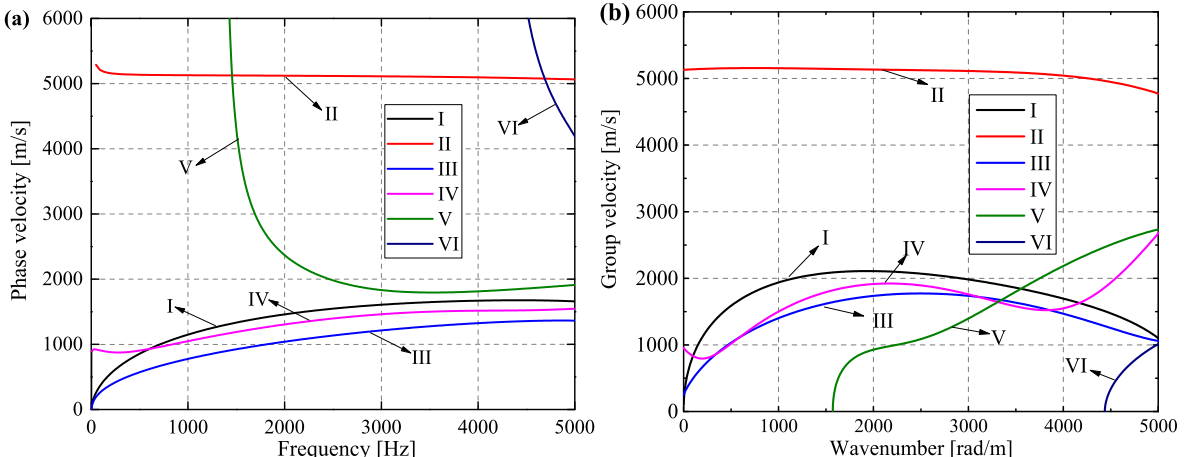


**Fig. 5.** Dispersion curves of (a) phase velocity and (b) group velocity.

approximately 5100 m/s matches well with the propagation velocity of compression waves in solid guides, which is  $\sqrt{E/\rho} = 5172 \text{ m/s}$ , where  $E = 210 \text{ GPa}$  and  $\rho = 7850 \text{ m/s}$  for the rail material.

Lateral bending waves (III) are dispersive waves, with the trends of phase and group velocities similar to those of vertical bending waves (I), but the values are approximately 300 m/s lower. Lateral torsion waves (IV) propagate at approximately 900 m/s at low frequencies. Above 500 Hz, the phase and group velocities of this type of wave follow a trend similar to those of vertical and lateral bending waves (I, III). Above 4000 Hz, there is a gradual increase in group velocity in comparison to the decrease in vertical and lateral bending waves (I, III).

At the cut-on frequency of web 1<sup>st</sup> bending waves (V), the wavenumber equals zero ( $k = 0$ ), and therefore, the phase velocity becomes infinite. As the frequency increases to 3 kHz, the phase velocity drops drastically to 1830 m/s. Then, it remains almost constant at higher frequencies. The group velocity rises significantly to 1000 m/s at 1710 Hz from 0 m/s at the cut-on frequency. At higher frequencies, it increases gradually to 2710 m/s. The phase and group velocities of web 2<sup>nd</sup> bending waves (VI) follow a trend similar to web 1<sup>st</sup> bending waves (V). Since the maximum frequency of interest is 5 kHz, only limited portions of these waves are shown in Fig. 5b.

### 3. Methods of experimental investigation

This section describes two experimental methods and compares them with the numerical simulation of the multimodal dispersive waves in a free rail. One method is operating deflection shape (ODS) measurement, which is used to distinguish between different wave modes. Then, the wavenumber-frequency curves of the waves are derived by postprocessing the ODSs and compare with those of the simulated waves. The other method is synchronized multiple-acceleration wavelet (SMAW) measurement, which is used to measure the propagation and dispersion characteristics of the waves. The group velocities in the vertical, longitudinal and lateral directions are estimated from the WPSs and compared with the FE simulation results.

#### 3.1. Sensor distribution

Lanza [34] applied a single-acceleration wavelet approach to study wave propagation in rails, as shown in Fig. 6a. This approach relied on the reflection signal from the rail ends to estimate the group velocities. Energy loss in the waves might occur during the reflection, leading to weak and less measurable signals, causing the signal-to-noise ratio to be too low and thus creating measurement error. Therefore, the SMAW approach is used in this work to avoid this potential error, as shown in Fig. 6b. More information about the wave propagation and dispersion along the rail is also expected from the multiple accelerometer measurement.

The ODS measurement also requires the simultaneous measurement of multiple accelerometers with a multichannel acquisition system [37]. The spatially equal accelerometer distribution is typically used for the convenience of data processing. The number of accelerometers determines the largest measurable wavenumbers of the modes. More accelerometers mean a larger wavenumber and higher wave wavenumber resolution but also a much higher cost. As a compromise, nine equally distributed accelerometers are used in this work, as shown in Fig. 6c.

The sensor distribution in Fig. 6c, together with a synchronized signal acquisition system, meets the demands for both the ODS measurement and the SMAW measurement and is applied in the following experimental setup.

#### 3.2. Experimental setup

Fig. 7 shows a schematic drawing of the experimental setup. A 4.97 m long rail was suspended in the air by two nylon ropes. Because of the small stiffness and damping levels of the ropes, the rail can be considered to be in 'free vibration'. Nine

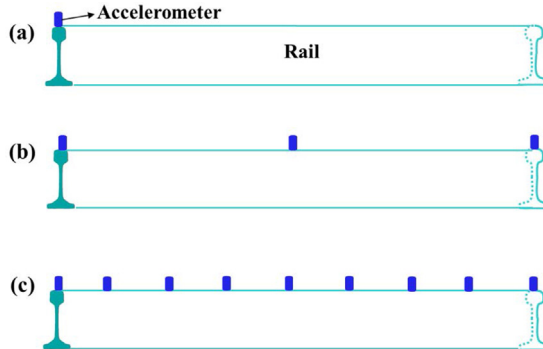


**Fig. 6.** Sensor distribution. (a) Single-acceleration wavelet for group velocity estimation in [34]; (b) SMAW approach for group velocity estimation in this paper; (c) sensor distribution for ODS measurement used in the real setup.

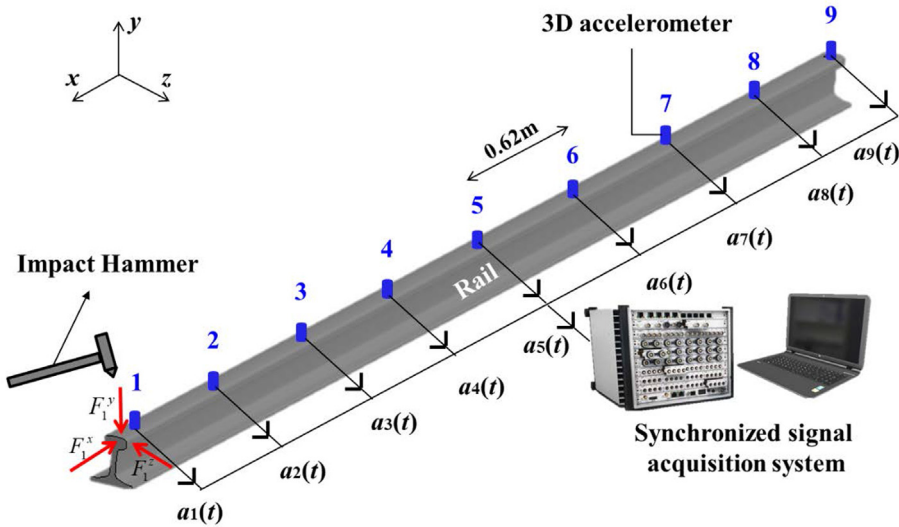


**Fig. 7.** Schematic drawing of the experimental setup.

3D accelerometers (PCB 356B21, denoted as 1–9 in Fig. 7) were glued onto the rail head with a spacing of approximately 0.62 m. The smallest wavelength of the measurable modes by this sensor distribution is twice the sensor spacing of 1.24 m, corresponding to the largest wavenumber of approximately 5.06 rad/m. The responses of the nine accelerometers are denoted as follows:

$$a_i(t) = [a_i^x(t), a_i^y(t), a_i^z(t)]^T, \quad i = 1, 2, \dots, 9 \quad (3)$$

where  $a_i(t)$  is the response of the  $i^{\text{th}}$  accelerometer, which includes three components  $a_i^x(t)$ ,  $a_i^y(t)$ , and  $a_i^z(t)$  in the longitudinal, vertical and lateral directions, respectively. The experimental setup is for both the ODS measurement and SMAW measurement. For the ODS measurement, accelerometers 1–9 were used. For the SMAW measurement, accelerometers 1, 5, and 9 were used.

A small impact hammer (PCB 086C03) with a steel tip was used to excite the rail in the high frequency range. The excitation positions were as close to 3D accelerometer 1 as possible for the longitudinal, lateral and vertical directions, as indicated by the red arrows in Fig. 7, and recorded as  $F_1^x(t)$ ,  $F_1^y(t)$ , and  $F_1^z(t)$ . The choice of the excitation positions at a rail free end is to ensure that excitation forces are not on a nodal line of any modal shape. The excitation and response signals of 5 impacts in each direction were recorded by a synchronized signal acquisition system with a sampling frequency of 51200 Hz. The reliable range of the impact forces and the repeatability of the signals were checked, and they were valid within 5 kHz.

### 3.3. Experimental methods

#### 3.3.1. ODS measurement method

The ODSs are measured from a set of FRFs. The FRFs in the longitudinal direction (x) can be calculated as follows [38]:

$$H_i^x(f) = \frac{S_{a_i^x F_1^x}(f)}{S_{F_1^x F_1^x}(f)(2\pi f)^2} \quad (4)$$

where  $H_i^x(f)$  is longitudinal FRF of accelerometer  $i$ ;  $S_{a_i^x F_1^x}$  is the cross-spectrum between the acceleration  $a_i^x(t)$  and force  $F_1^x$ ; and  $S_{F_1^x F_1^x}$  is the auto-spectrum of the force  $F_1^x$ . The FRFs are complex-valued functions. The ODSs of rail displacement responses are taken as the spatial distribution of the imaginary parts of the FRFs, as follows [37].

$$\text{ODS}_x(f) = [\text{Im}(H_1^x(f)), \text{Im}(H_2^x(f)), \dots, \text{Im}(H_9^x(f))] \quad (5)$$

where  $\text{ODS}_x(f)$  is the longitudinal ODS at frequency  $f$ . When the frequency is one of the rail natural frequencies, the ODS will closely approximate the mode shape [37]. The lateral and vertical FRFs and ODSs can be obtained with the same method.

Fig. 8 shows one example to explain the procedure of the ODS measurement for modal identification. First, a set of vertical FRFs at the nine positions are obtained with the hammer test, as shown in Fig. 8a and 8b. Second, the resonance peaks at 492 Hz (indicated by red dashed circles in Fig. 8b) are detected from the magnitude of the FRFs, which may correspond to one or more natural rail modes. Third, the imaginary parts of the FRFs at this peak frequency at the nine positions are derived, as depicted in Fig. 8c. Last, the ODS is taken as their spatial distribution along the rail, as shown in Fig. 8d. By com-

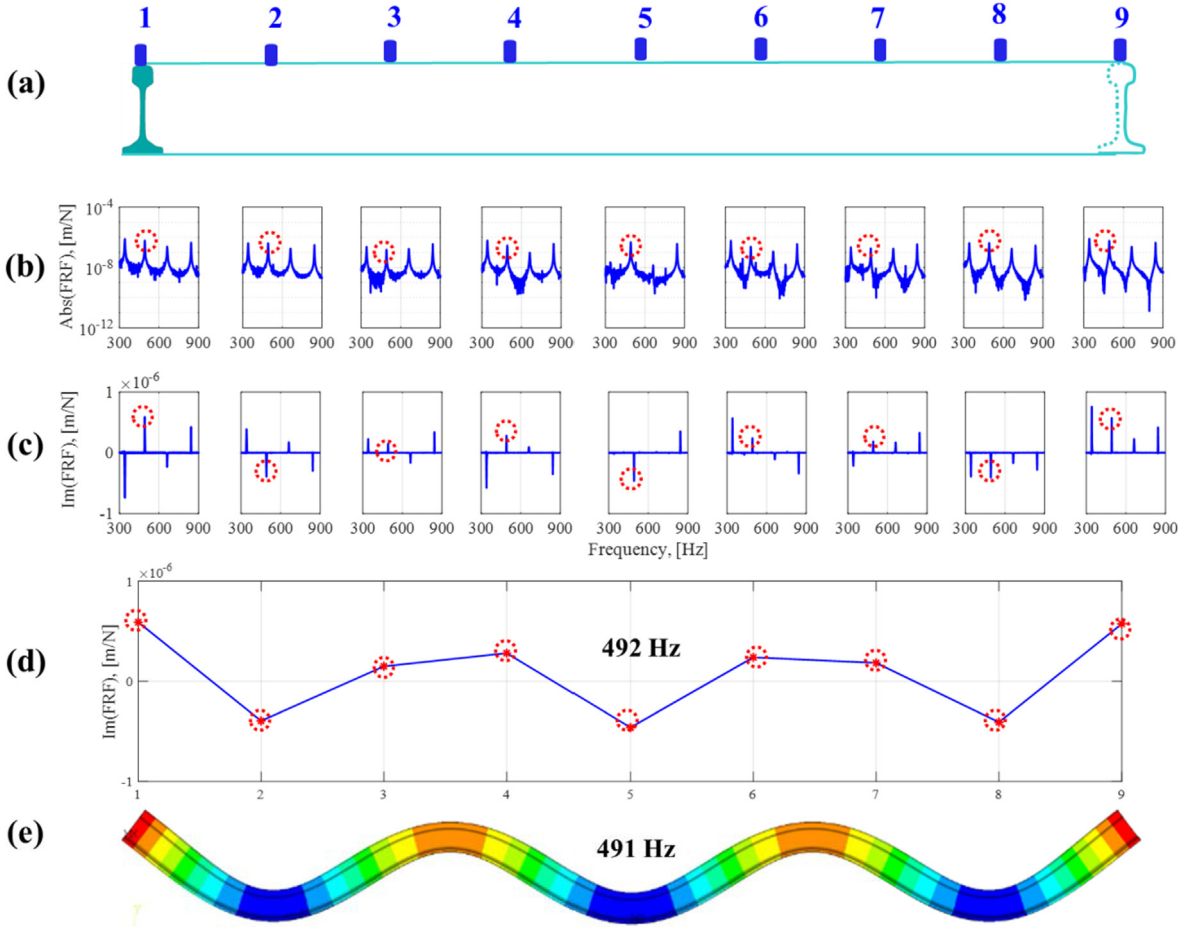


**Fig. 8.** ODS measurement at 492 Hz for modal identification. (a) Sensor distribution of hammer test; (b) magnitude of FRFs at nine positions; (c) imaginary parts of FRFs at nine positions; (d) measured ODS at 492 Hz; (e) simulated mode shapes at 491 Hz. The red circles in (b) and (c) indicate the detected peaks at 492 Hz. (For interpretation of the references to color in this figure legend, the reader is referred to the web version of this article.)

paring the measured peak frequency and ODS with the simulated natural frequency and mode shape (see Fig. 8e), one vertical vending mode at 491 Hz in the FE simulation is identified. Other rail modes can be identified with the same procedures.

After deriving the peak frequencies and ODSs from FRFs, the wavenumber-frequency curves can be obtained and compared with the simulated curves.

### 3.3.2. SMAW measurement method

Wave propagation signals along the rail under an impulsive hammer excitation are nonstationary and contain many frequency components. To address this kind of signal, the continuous wavelet transform (CWT) is applied. In the CWT, the convolutions of the analyzed signal are calculated with a group of scaled and shifted wavelet functions. The wavelet coefficients  $W_n(s)$  of the analyzed signal  $x_n$  can be represented as follows [39]:

$$W_n(s) = \sum_{n'=0}^{N-1} x_{n'} \psi^* \left[ \frac{(n'-n)\delta_t}{s} \right] \quad (9)$$

where  $\Psi$  is the mother wavelet,  $s$  is the wavelet scale,  $N$  is the number of points in the time series,  $n' = 0, \dots, N - 1$ ,  $\delta_t$  is the time step,  $n$  is the continuous variable for the translation,  $s$  is the wavelet scale,  $*$  presents a complex conjugate and  $\psi^* \left[ \frac{(n'-n)\delta_t}{s} \right]$  is a family of wavelets deduced from the mother wavelet by various translation and scaling steps. Here, the Morlet function is employed as the mother wavelet [40]. The wavelet power spectrum (WPS) is calculated by  $|W_n(s)|^2$ . The SMAW measurement refers to the measured WPSs of synchronized accelerations at positions 1, 5 and 9.

An algorithm to estimate group velocity from the WPSs is developed, as shown in Fig. 9a.

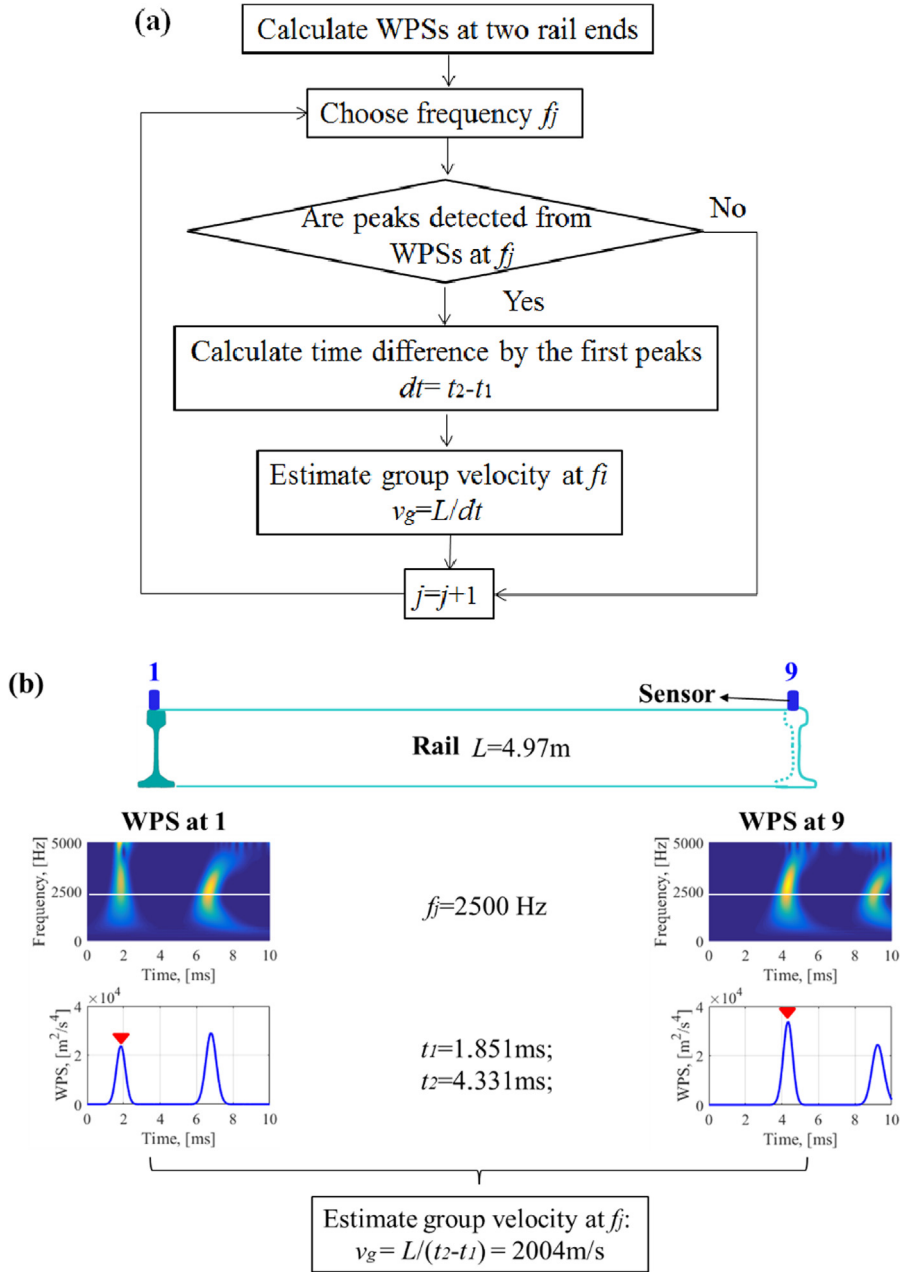


**Fig. 9.** The algorithm of group velocity estimation from WPSs: (a) the flowchart of the algorithm; (b) one example of the algorithm. The white line in (b) shows WPSs at 2500 Hz. The red triangles indicate the detected first peaks from WPSs at 2500 Hz. (For interpretation of the references to color in this figure legend, the reader is referred to the web version of this article.)

First, WPSs of acceleration signals at the two rail ends are calculated. Then, one frequency  $f_j$  (i.e., 2500 Hz) is chosen in the WPSs, as indicated by the white solid lines in Fig. 9b. The first peaks at time  $t_1$  and time  $t_2$  are detected from the WPSs at these two positions (see the red triangles), which indicate the first arrival of the wave. There is a time difference  $dt$  between these two peaks, during which time the waves propagate through one rail length ( $L$ ). Therefore, the group velocity at  $f_j$  is calculated as follows:

$$v_g = \frac{L}{(t_2 - t_1)} \quad (10)$$

Afterward, we move to the next frequency  $f_{j+1}$  and repeat the procedure above. At some frequencies, the vibration energy of the waves is small, and the obvious peaks, as in Fig. 9b, may not be accurately detected from the WPSs. For these cases, the group velocity at these frequencies cannot be estimated accurately or cannot be measured at all.

## 4. Experimental results

### 4.1. Results of ODS measurement

Fig. 10 shows the vertical, longitudinal and lateral FRFs of the rail at accelerometer 1. There are many peaks of the FRF in each direction, which can be classified into ‘major peaks’ and ‘minor peaks’. Major peaks ( $\star$ ) of the longitudinal FRF (Fig. 10b) refer to longitudinal compression modes, while minor peaks ( $\blacklozenge$ ) refer to other modes, e.g., vertical bending modes (see black dashed lines in Fig. 10a and 10b for examples). The appearance of minor peaks comes from the mode coupling of the different directions. Major and minor peaks can be distinguished by peak frequencies and the corresponding ODSs. Fig. 10c shows the coupling of four groups of major peaks, representing lateral bending, lateral torsion, web 1<sup>st</sup> bending and web 2<sup>nd</sup> bending modes. Specifically, two groups of major peaks at 0–1560 Hz correspond to lateral bending and torsion modes, and at approximately 1560 Hz and 4400 Hz, with the supplement of web 1<sup>st</sup> and 2<sup>nd</sup> bending modes (indicated by two black arrows, respectively).

The results of the ODS measurement are derived and shown in Fig. 11. All six types of rail modes predicted from the FE model are identified by the ODSs. Three examples are chosen for each type and compared to the modal results of the numerical simulation. The simulated natural frequencies and mode shapes agree well with the measured peak frequencies and the corresponding ODSs. It should be noted that the smallest wavelength that can be measured by the ODSs is 1.24 m, with an accelerometer spacing of 0.62 m. The modes with wavelengths smaller than 1.24 m could be measured by reducing the accelerometer spacing, which was not included in this paper.

Based on the results of the ODS measurement, the dispersion curves are measured by connecting the discrete wavenumber-frequency points (see Fig. 12). Among them, points ( $\circ$ ) of wavenumbers below 5.06 rad/m ( $2\pi/1.24$ ) are derived directly from the ODSs. For points ( $\triangle$ ) of higher wavenumbers, their natural frequencies are derived from the major peak frequencies of FRFs. The latter may require further comparison from measurements with a more dense accelerometer arrangement. Comparing the measured dispersion curves with the simulation, very good agreement was found in the frequency range of 0–5 kHz, except for a slight overestimation (1.3%) for the web 2<sup>nd</sup> bending wave (VI) of the FE model. The good agreement also verifies that the cross-section size of 4 mm and the longitudinal element size of 10 mm are accurate

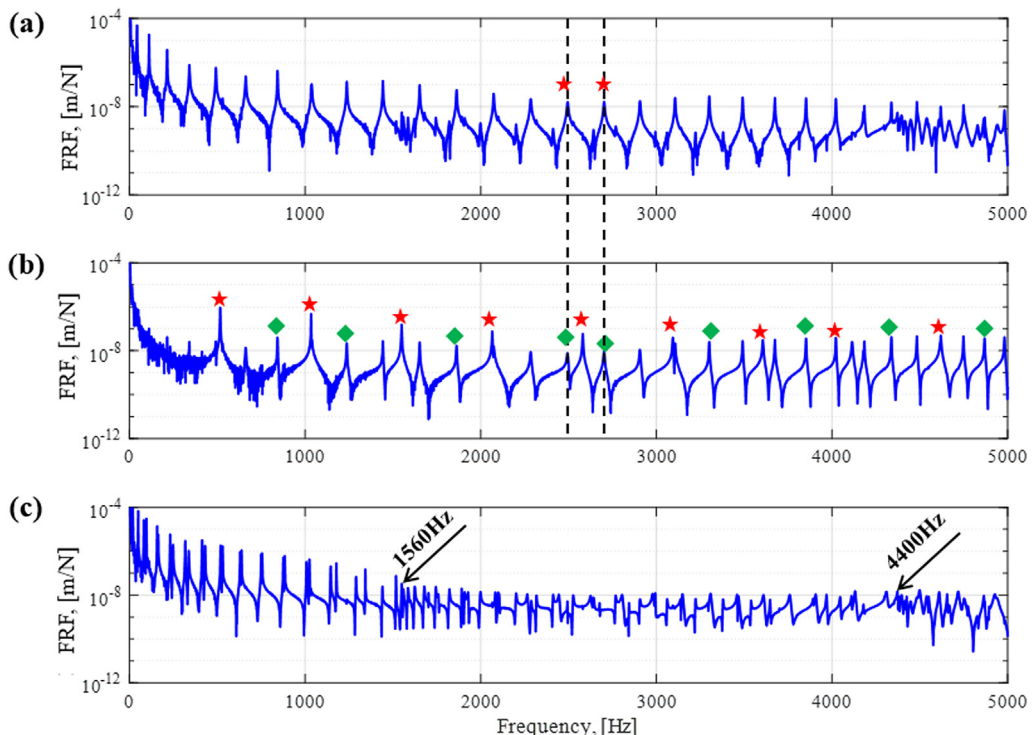


**Fig. 10.** (a) Vertical, (b) longitudinal, (c) lateral FRFs of rail at accelerometer 1. ( $\star$ ) indicates major peaks; ( $\blacklozenge$ ) indicates minor peaks.

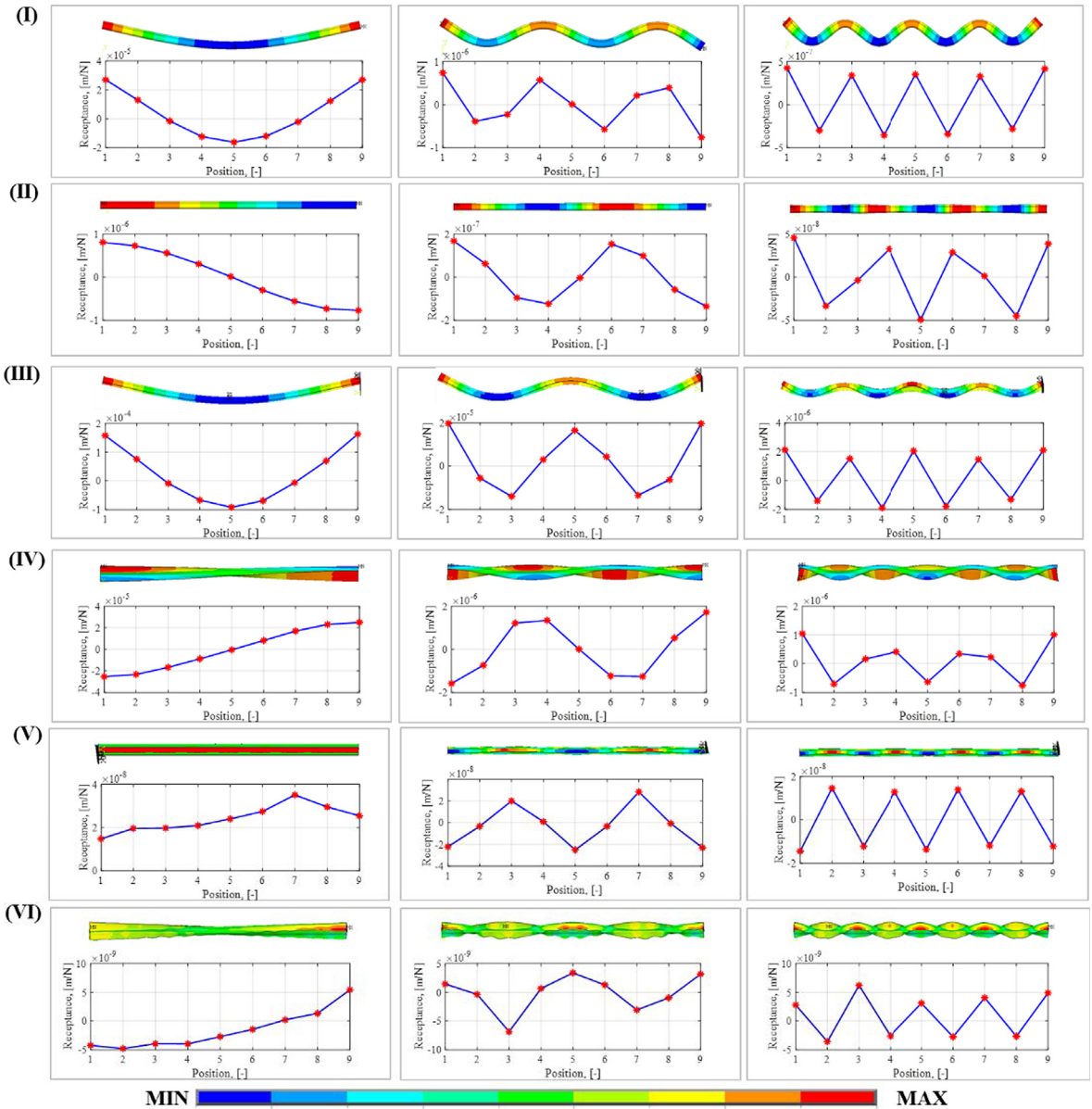


**Fig. 11.** Comparison between the mode shapes from FE simulation ('Worn 1' in A. 3) and ODSs from measurement (I) vertical bending modes at 42/43 (simulation/measurement), 345/341, 845/843 Hz, (II) longitudinal compression modes at 515/517, 1545/1550, 3084/3095 Hz, (III) lateral bending modes at 18/18, 97/97, 416/414 Hz, (IV) lateral torsion modes at 81/82, 246/248, 527/530 Hz, (V) web 1<sup>st</sup> bending modes at 1570/1555, 1693/1681, 2008/2000 Hz, (VI) web 2<sup>nd</sup> bending modes at 4440/4383, 4505/4448, 4718/4666 Hz.

enough for studying rail dynamic behavior within 5 kHz, and the measured rail height can achieve a better solution than the nominal height, with the largest difference being 3.8%.

#### 4.2. Results of SMAW measurement

The WPSs for vertical signals at accelerometers 1, 5 and 9 are shown in Fig. 13a, 13b and 13c, respectively. The color contrast indicates the amount of energy concentrated in a frequency range (the vertical axis) at a particular time (the horizontal axis). The shapes of the wave envelope are captured from the WPSs. The wave envelope propagation along the rail can be clearly seen: at time  $t_{1z}$ , the impulsive hammer is excited on the rail close to accelerometer 1; then, the energy envelope propagates to accelerometer 5 at time  $t_{2z}$  and to accelerometer 9 at time  $t_{3z}$ ; after that, the waves reflect at accelerometer 9 and return to accelerometer 5 at time  $t_{4z}$  and to accelerometer 1 at  $t_{5z}$ . From  $t_{1z}$  to  $t_{5z}$ , the wave envelope finishes a cycle, and the propagation distance is twice the rail length ( $2L$ ).

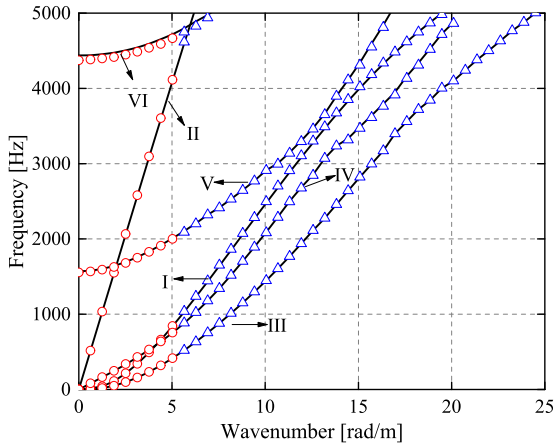


**Fig. 12.** Wavenumber-frequency dispersion curves: (—) FE simulation ('Worn 1' in A. 3); (○) wavenumber-frequency points derived from ODSs; (Δ) the points with measured natural frequencies and predicted wavenumbers.

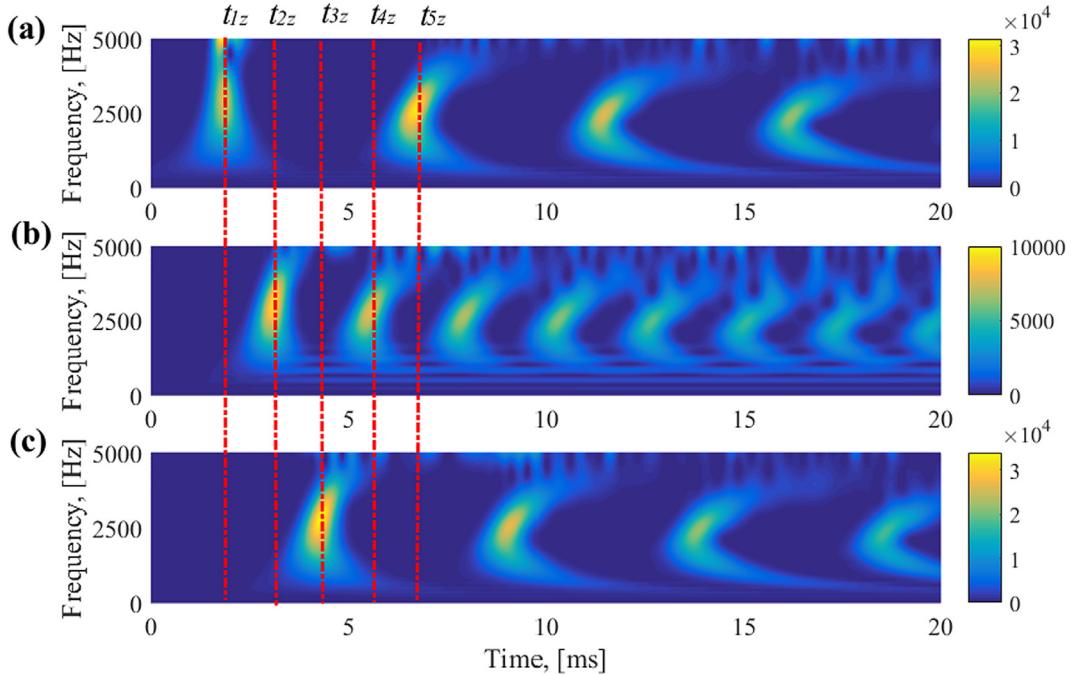


**Fig. 13.** WPSs of vertical signals at (a) accelerometer 1, (b) accelerometer 5 and (c) accelerometer 9. The red dashed lines indicate the selected time. (For interpretation of the references to color in this figure legend, the reader is referred to the web version of this article.)

During wave propagation, the shapes of the wave envelope change due to the dispersive characteristics of the rail—the dependence of velocity on frequency. With increasing time, the wave gradually takes a 'C' shape, qualitatively indicating that the vertical wave velocity (group velocity) in the middle frequency range is higher than those in the lower and higher frequency ranges, which agrees with the calculated results in Fig. 5b. The shape at time  $t_{1z}$  at accelerometer 1 is relatively irregular because of the near field waves.

Wave energy densities at accelerometers 1 and 9 are similar and significantly larger than those at accelerometer 5, which indicates that the vibrations at the two rail ends are stronger because of the free boundaries. In addition, the wave energy at the three positions is attenuated during propagation, as observed from the increasingly dark color of the wave envelope.

The WPSs for the longitudinal and lateral signals are shown in Fig. 14 and Fig. 15. Waves in these two directions have propagation traces similar to the vertical ones, but it can be clearly seen that the longitudinal group velocity is larger than those of the vertical and lateral waves. From the numerical results in Section 2.4, it can be predicted that the shapes of the

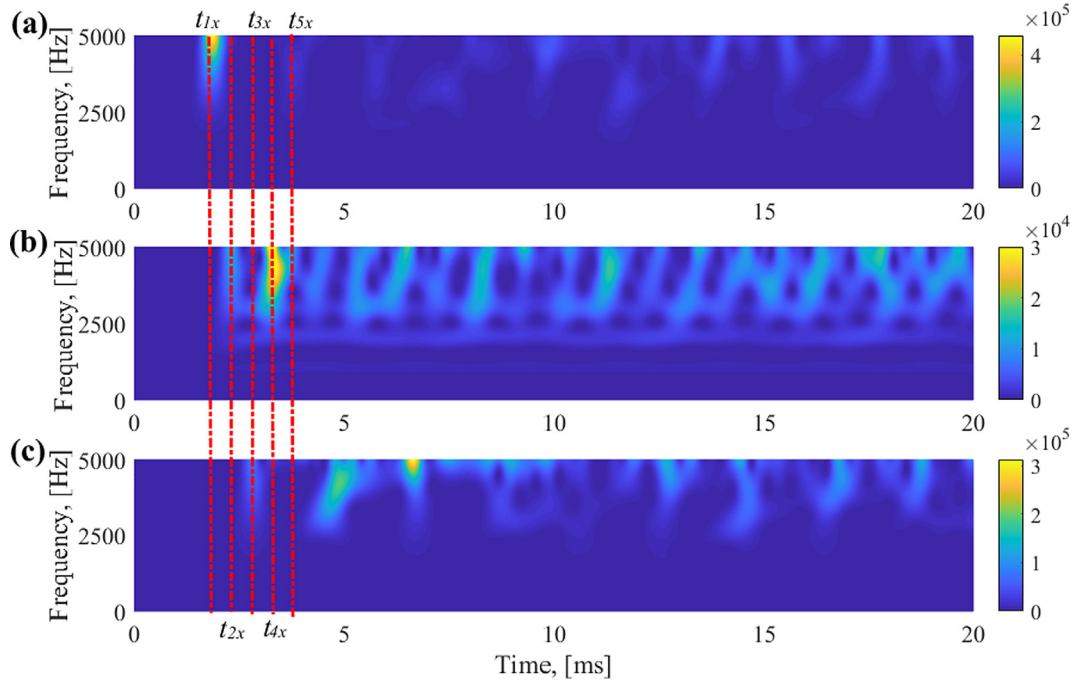


**Fig. 14.** WPSs of longitudinal signals at (a) accelerometer 1, (b) accelerometer 5 and (c) accelerometer 9. The red dashed lines indicate the selected time. (For interpretation of the references to color in this figure legend, the reader is referred to the web version of this article.)

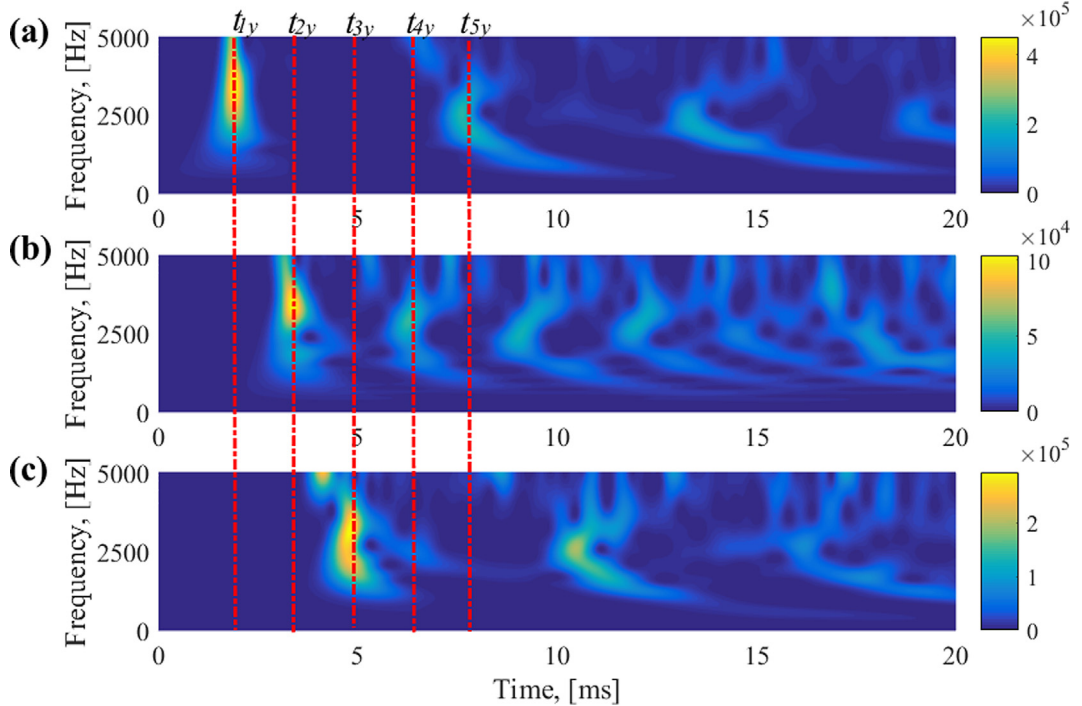


**Fig. 15.** WPSs of lateral signals at (a) accelerometer 1, (b) accelerometer 5 and (c) accelerometer 9. The red dashed lines indicate the selected time. (For interpretation of the references to color in this figure legend, the reader is referred to the web version of this article.)

longitudinal wave envelopes should not change with propagation, since the longitudinal group velocity is frequency-independent within 5 kHz. However, moderate deformation is observed in Fig. 14, which may be caused by signal coupling from other directions, which is also shown in Fig. 10b. The lateral wave envelopes deform with time and have a shape similar

to the vertical ones. The shapes of the lateral waves at high frequencies are quite irregular, which is likely caused by the superposition of the four types of lateral waves.

The group velocities for the vertical, longitudinal and lateral waves are presented in Fig. 16. The measured vertical group velocity curve agrees well with that of the simulation in the frequency range of 400–3500 Hz. From 3500 to 4200 Hz, the numerical results underestimate the velocity slightly. Below 400 Hz and above 4200 Hz, the vertical vibration energy is too low (see Fig. 13 to identify the peaks from the WPSs accurately). Good agreement of the measured and simulated longitudinal group velocity is achieved in the frequency range of 900 Hz–5 kHz. The velocity below 900 Hz cannot be obtained precisely with lower vibration energy (see Fig. 14a). The measured lateral group velocity coincides well with that of the simulated lateral bending waves (III) in the frequency range of 200–3800 Hz. This means that the lateral bending waves dominate the rail head vibration in this frequency range. At frequencies above 3800 Hz, the measured group velocity curve does not follow that of any single type of wave but stays between web 1st bending waves (V) and the other three types. It is likely that in this frequency range, the four types of waves contribute together to the rail head vibration. In summary, good agreement between the simulated and measured group velocities has been achieved, indicating that the 3D FE model can accurately predict the propagation and dispersion of waves in a free rail.

Compared to the experimental results by the single-acceleration wavelet approach in [34], the proposed SMAW approach better presents the wave propagation and dispersion along the free rail with multiple synchronized WPSs. The valid frequencies of group velocity estimation are also extended to a broader frequency range owing to the higher signal-to-noise ratio.

## 5. Discussion

In this section, we discuss the advantages and disadvantages of ODS measurements and SMAW measurements and the effectiveness of these two methods in field tracks based on preliminary experimental results.

### 5.1. Discussion of ODS and SMAW measurement

The experimental results of the ODS and SMAW measurements are both in good agreement with the simulation results, which indicate these two approaches are capable of distinguishing wave modes and measuring wave propagation and dispersion characteristics. The ODS and SMAW measurement methods have their own respective advantages and disadvantages. ODS measurement is able to identify all types of rail modes and distinguish between them easily from their wavelengths. SMAW measurements can only identify waves that have prominent vibration energy. Therefore, arrangements of the sensors at different locations of the rail cross-section (e.g., the middle part of rail web) will be helpful to identify different waves (e.g., web 1st bending waves). The advantage of SMAW measurement is its capability to obtain continuous dispersion curves, while only the discrete frequencies can be measured by ODS measurement. In addition, SMAW measurements are easier to implement since fewer 3D accelerometers are required. The sensor distribution in ODS measurement is relatively more complex, and the number of accelerometers necessary is determined by the expected wavenumber resolution.

### 5.2. The effectiveness of ODS measurement and SMAW measurement in field track

The experimental and simulation results above have indicated that ODS measurement and SMAW measurement are capable of identifying the coupled vibration modes and deriving the wave dispersion characteristics of a free rail. In this section,

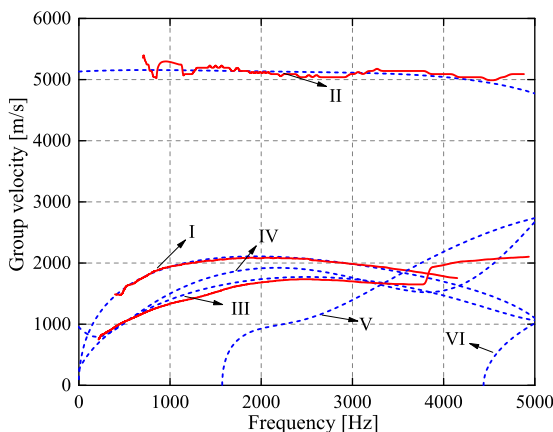


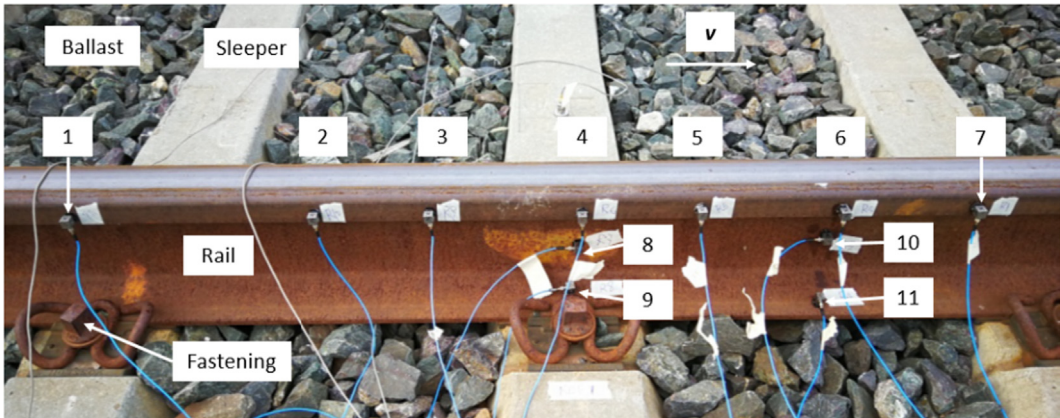
**Fig. 16.** Comparison of the group velocity dispersion curve between SMAW measurement and FE simulation: (—) measurement; (---) simulation.

we applied these two experimental methods in field railway tracks to evaluate their effectiveness on rails with real boundary conditions.

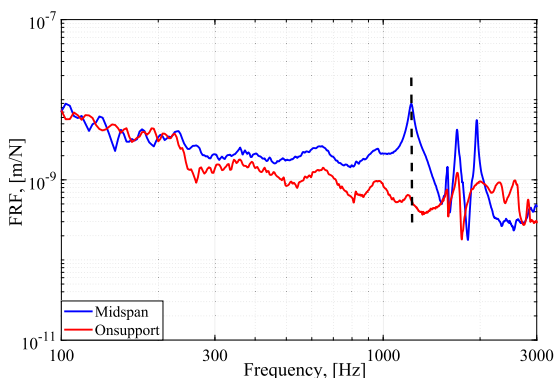
The experimental setup is shown in Fig. 17. The track without visible defect is in Railway Testing center Faurei, Romania. The UIC60 E1 rail was constrained by Vossloh W14 fastenings on prestressed monoblock sleepers every 0.6 m. No joints, welds and crossings are nearby. The track can thus be considered as effectively infinite. Eleven 3D accelerometers (PCB 356B21, denoted as 1–11 in Fig. 17) were used to measure the rail vibrations under the impact of the hammer. Accelerometers 1–7 were glued onto the rail head on the field side. Among them, accelerometers 1 and 4 were above the sleeper (called on-support below); accelerometers 2 and 6 were at the mid-span of the rail; and accelerometers 3, 5 and 7 were at the quarter-span. Accelerometers 8 and 10 were glued onto the rail web, and accelerometers 9 and 11 were glued onto the rail foot.

Fig. 18 shows the measured vertical FRFs at mid-span (Position 2) and on-support (Position 4). The FRFs in form of receptance are calculated by the measured accelerations and hammer forces. From the FRF, the track appears to have quite stiff railpads [13]. A series of peaks and dips were observed in the FRFs, which correspond to the track resonance or anti-resonance modes [5,22,24]. Among them, one peak at 1240 Hz (as indicated by the dashed line) may correspond to rail vertical pinned-pinned resonance [5,24], which is the vertical banding mode with a wavelength of twice the sleeper space; see the mode shape in Fig. 19a. To identify the rail modes corresponding to this peak, the ODS at 1240 Hz from accelerometers 1–7 was derived and fitted by a sine curve, as shown in Fig. 19b. The shape of the measured ODS agrees well with the mode shapes of the pinned-pinned resonance, indicating that the peak at 1240 Hz corresponds to the pinned-pinned resonance. From this example, ODS measurement is a possible method to identify rail vibration modes in field tracks. It is worth noting that the rail in field tracks has mostly propagating waves instead of the standing waves. Due to the track damping, the wavenumbers of the propagating waves have both the real and imaginary parts. The identification of these wave modes requires to consider both their real and imaginary parts from ODS measurement. These potentially make it more challenging to identify the waves by ODS measurement in the field track.

The WPSs for vertical signals at accelerometers 1, 4 and 7 are shown in Fig. 20a, 20b and 20c, respectively. The excitation position of the hammer was as close as possible to accelerometer 1. Fig. 20 shows that the wave envelope propagated from



**Fig. 17.** Experimental setup of ODS and SMAW measurements in the field track.



**Fig. 18.** Measured vertical FRFs at mid-span and on-support. The black dashed line indicates the frequency at 1240 Hz.

accelerometer 1 to accelerometer 7, and its shape changed during this process due to wave dispersion. Compared to the results of the free rail in Fig. 13, wave reflection was not observed in the field track, which should be caused by track damping that significantly attenuates the vibrational waves. This result also shows the advantage of the SMAW approach over the single-acceleration wavelet approach, which does not depend on the reflection signal from the rail ends to measure the group velocities. In addition, the wave envelope in the field track concentrates at a higher frequency range above

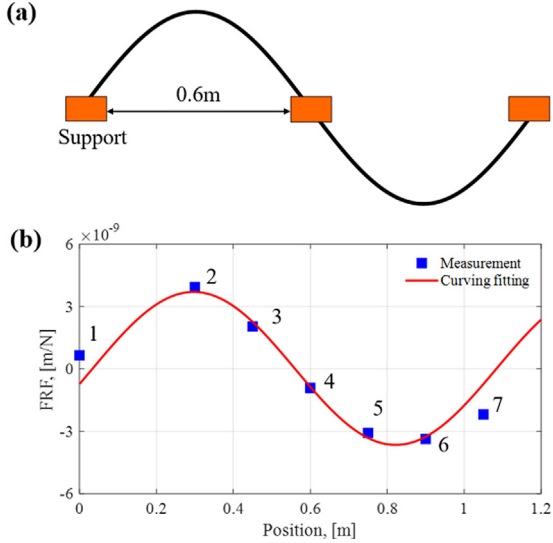


**Fig. 19.** Mode shape and ODS of pinned-pinned resonance. (a) Mode shape of pinned-pinned resonance; (b) (■) Measured ODS at 1240 Hz; (—) sinusoidal curving fitting of ODS.

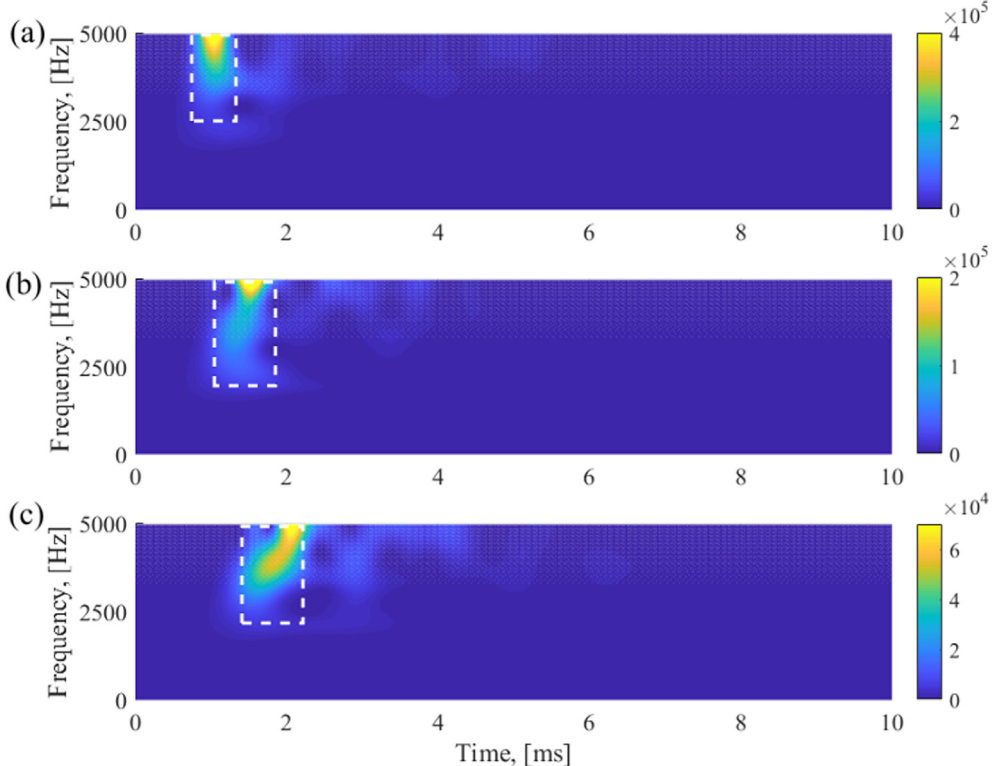


**Fig. 20.** WPSs of vertical signals at (a) accelerometer 1, (b) accelerometer 4, and (c) accelerometer 7.

2500 Hz, as indicated by the white dashed rectangle in Fig. 20, while that of the free rail concentrates at 200 Hz–5 kHz. This may indicate that the support stiffness of the rail in the field track significantly suppresses rail vibrations at a lower frequency than 2500 Hz and leads to a higher decay rate. Using the 3D FE track model developed in [13], numerical simulation results indicated that the velocity signal is more sensitive to the rail vibration at lower frequencies than the acceleration signal. If the rail vibration at lower frequencies is of significant interest, the SMAW measurement of velocity can be better than that of acceleration.

In summary, this section presents preliminary results of ODS measurements at vertical pinned–pinned resonance peaks and SMAW measurements of vertical bending waves in field tracks. From these results, ODS measurements can be used to identify vibration modes and SWAM measurements can be applied for the wave propagation and dispersion analysis of the rail in field tracks. More experimental evidence may be needed to support the conclusions, which will be provided in future work.

## 6. Conclusions and future work

In this paper, we present a solution method based on FE modeling to predict the multimodal dispersive waves in a free rail at a frequency range of 0–5 kHz. Six types of waves are extracted in the vertical, longitudinal and lateral directions. The phase and group velocities of these waves are derived and discussed in detail and provide useful information to understand wave propagation and dispersion along the rail. Their modal behavior and wavenumber-frequency dispersion relations are also obtained and are found to be similar to the simulation results in the literature [9,12].

The ODS measurement is conducted to distinguish between different types of wave modes. Experimental results indicate that all six types of wave modes are identified by the ODS. Good agreement is achieved between the simulated mode shapes and the measured ODSs. The wavenumber-frequency dispersion relations are also derived by postprocessing the ODS results and have the largest deviation of only 3.8% compared with the simulated ones.

An SMAW approach is developed and applied to study the dispersive waves in the free rail. The propagation and dispersion of the vertical, longitudinal and lateral waves are measured from the WPSs. An algorithm is also developed to estimate the group velocities from the WPSs. Good quantitative agreement is achieved between the simulated and measured results of the vertical bending waves, longitudinal compression waves and lateral bending waves, indicating that the 3D FE model can accurately predict the propagation and dispersion of waves in a free rail.

In summary, this work contributes to a better understanding of free rail vibrations and illustrates the effectiveness of the ODS measurement for rail modal identification and SMAW measurement for wave dispersion analysis. For the ODS measurement, more accelerometers could be mounted in the longitudinal direction to obtain higher spatial resolution. More accelerometers could also be used on each cross-section to capture the cross-section deformation of the wave modes.

## CRediT authorship contribution statement

**Pan Zhang:** Conceptualization, Methodology, Software, Formal analysis, Data curation, Investigation, Writing – original draft, Writing – review & editing, Visualization. **Shaoguang Li:** Validation, Investigation, Software, Writing – review & editing. **Alfredo Núñez:** Methodology, Writing – review & editing, Visualization, Supervision, Funding acquisition. **Zili Li:** Conceptualization, Methodology, Resources, Writing – review & editing, Supervision, Project administration, Funding acquisition.

## Declaration of Competing Interest

The authors declare that they have no known competing financial interests or personal relationships that could have appeared to influence the work reported in this paper.

## Acknowledgements

This work was partly supported by the China Scholarship Council. The authors of this paper appreciate the detailed, critical, and constructive comments of the reviewers.

## Appendix A. Influencing factors of the numerical simulation

In the appendix, three influencing factors of FE simulation on obtaining wave dispersion relations, meshing, rail lengths and rail heights, are studied.

### Meshing

Three cross-section discretization variation schemes are employed. The rail cross-section profile is discretized with equal element edge sizes of 16 mm, 8 mm and 4 mm. The longitudinal element sizes are varied, including 50 mm, 20 mm and 10 mm. Five simulation cases are tested and listed in Table A1.

**Table A1**  
Description of simulation cases.

Case	Cross-section discretization size (mm)	Longitudinal size (mm)
1	16	20
2	8	20
3	4	20
4	4	50
5	4	10

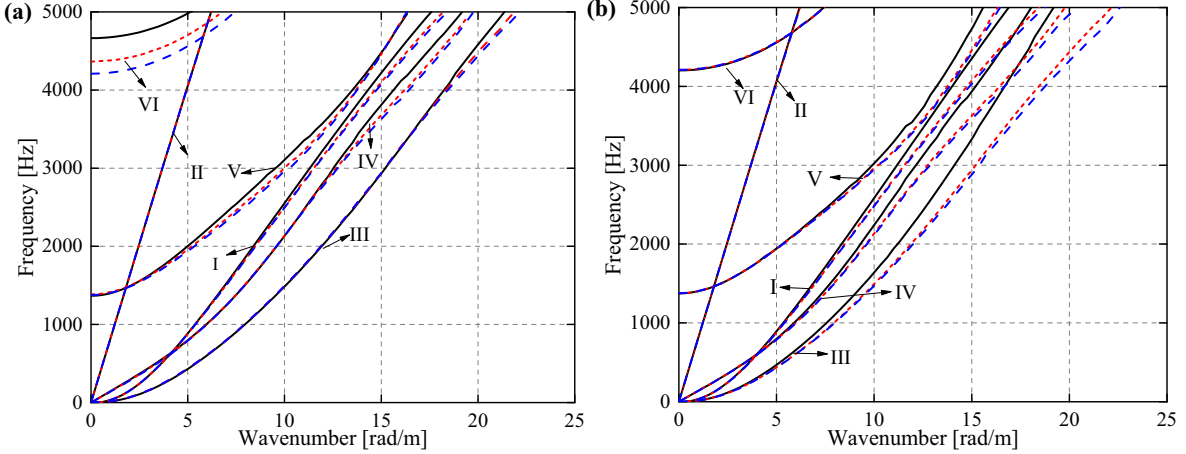


**Fig. A1.** Dispersion curves of different (a) cross-section discretization size case 1 (—); case 2 (---); case 3 (—); (b) longitudinal element size case 3 (—); case 4 (---); case 5 (—).

Fig. A1a shows the results of cases 1, 2, and 3 to study the influence of the cross-section discretization size. For cases 2 and 3, the wavenumber-frequency curves overlap almost completely with each other, with web 2nd bending waves (VI) having the largest deviation of 3.6%. Further finer mesh is advisable to improve the accuracy for waves (VI). Considerable differences up to 10.8% between cases 1 and 3 are observed for vertical bending waves (I), lateral bending waves (III), lateral torsion waves (IV), web 1<sup>st</sup> bending waves (V), and web 2<sup>nd</sup> bending waves (VI) when the frequencies are higher than 1711 Hz, 3756 Hz, 2657 Hz, 1584 and 4209 Hz, respectively, where significant cross-section deformations for them have been observed in Fig. 3. Different from other types of waves, longitudinal compression waves (II) are not sensitive to this mesh difference since no cross-section deformation occurs below 5 kHz (see Fig. 3).

The results of cases 3, 4, and 5 are shown in Fig. A1b to determine the influence of the longitudinal element size. The wavenumber-frequency curves of cases 3 and 5 overlap almost completely with each other, with the largest deviation being 2.5%. Significant differences up to 21.2% between cases 4 and 5 are observed for vertical bending waves (I), lateral bending waves (III), lateral torsion waves (IV), and web 1<sup>st</sup> bending waves (V) when the wavenumber is higher than approximately 10 rad/m. Longitudinal compression waves (II) and web 2<sup>nd</sup> bending waves (VI) whose maximum wavenumbers up to 5 kHz are below 10 rad/m are not sensitive to longitudinal element size. The reason is that the longitudinal element size determines the wavenumber resolution and thus has a more significant influence on waves with larger wavenumbers.

Overall, longitudinal compression waves (II) are influenced neither by cross-section discretization size nor by longitudinal element size. Web 2<sup>nd</sup> bending waves (VI) are mainly affected by the former. The other four waves, vertical bending waves (I), lateral bending waves (III), lateral torsion waves (IV), and web 1<sup>st</sup> bending waves (V), are all sensitive to both factors. Additionally, if the allowable error is not larger than 3.6%, a cross-section discretization size of 8 mm and a longitudinal element size of 20 mm can be a good compromise between the accuracy and computation time for studying the dispersive waves in the rail in the frequency range of 0–5 kHz.

#### Rail length

Three different rail lengths of 15 m, 10 m, and 5 m are studied in the FE model. All three models use a nominal UIC 54E1 rail profile, and a cross-sectional mesh size of 4 mm and longitudinal element size of 10 mm are applied to obtain the best accuracy. The results of these three cases are shown in Fig. A2. The wavenumber-frequency curves are almost identical. Fig. A2b shows discrete wavenumber-frequency points (corresponding to characteristic modes) of longitudinal compression waves (II). In the same frequency range, more points occur with longer rail.

Overall, the rail length does not influence the dispersion relations of the rail but changes the number of characteristic modes. Therefore, from the experimental point of review, we can conclude that a rail length (e.g., 4.97 m in this paper) is appropriate to derive dispersion curves of the rail. However, it should be noted that rail vibration modes will be influenced by the choice of different rail lengths.

### Rail height

A 4.97 m rail, taken from the Dutch railway after long-term service, was measured in 3D with a HandyScan (see Fig. A3a). The precision of the HandyScan is 30  $\mu\text{m}$  in arbitrary directions. The measured rail is shown in Fig. A3b and compared with the nominal UIC 54E1 rail in Fig. A4a. The most significant difference is the rail head height, with the measured height being 5.8 mm lower than the nominal height. The rail web and rail foot show little difference between the measured and nominal profiles.

The measured rail profile (called 'Worn 1' below) and nominal UIC 54E1 profile (called 'Nominal' below) are both used as inputs to the FE models. To further study the influence of rail height, a reduction of 12 mm (called 'Worn 2' below) compared to nominal UIC 54E1 (see Fig. A4a) is also modeled. The model length is 4.97 m, a cross-section mesh size of 4 mm and a longitudinal element size of 10 mm are applied. The results of these three cases are shown in Fig. A4b. The most significant differences in the wavenumber-frequency curves are observed for web 2<sup>nd</sup> bending waves (VI), with the largest deviation of 10.4% between nominal and 'Worn 2'. Visible differences occur at higher frequencies for lateral bending waves (III) and torsion waves (IV) and cut-on frequencies of web 1<sup>st</sup> bending waves (V). For these three cases, the wavenumber-frequency curves of vertical bending waves (I) and longitudinal compression waves (II) agree with each other well.

Overall, the four types of lateral waves are all sensitive to rail height degradation because considerable cross-section deformations are observed in Fig. 3. Therefore, for research on rolling noise problems that are strongly influenced by rail lateral vibration, it is advisable to model the rail with measured rail height to correlate numerical results better with field noise

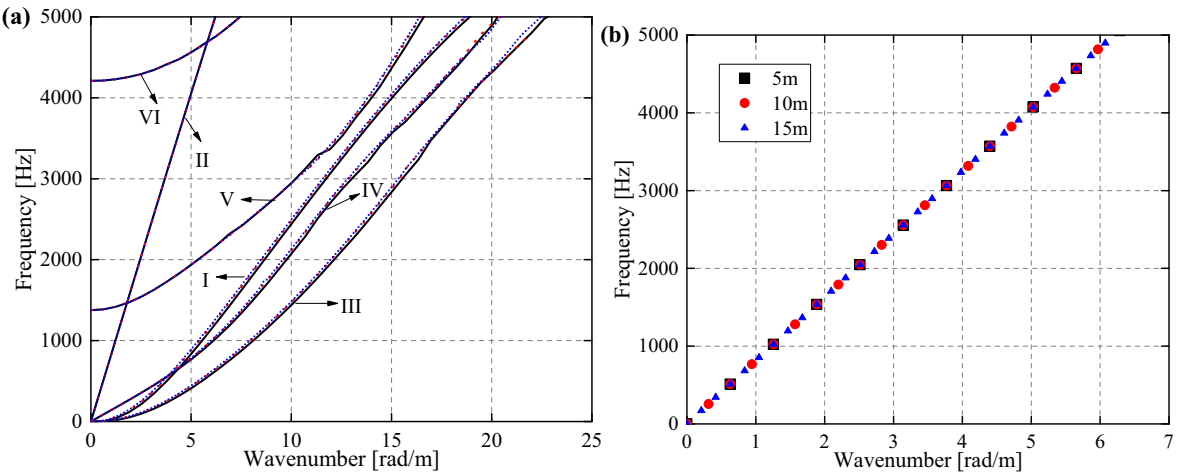


**Fig. A2.** Wavenumber-frequency relations of (a) 5 m (—); 10 m (---); 15 m (----). (b) Longitudinal modes.

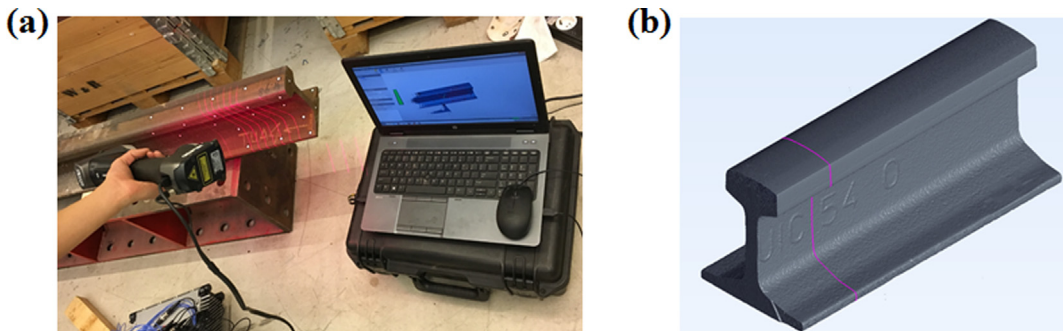


**Fig. A3.** Rail profile measurement. (a) Measurement by HandyScan, (b) Measured rail profile. The pink dashed line is a selected rail cross-section indicated as 'Worn 1' in Fig. A4a.

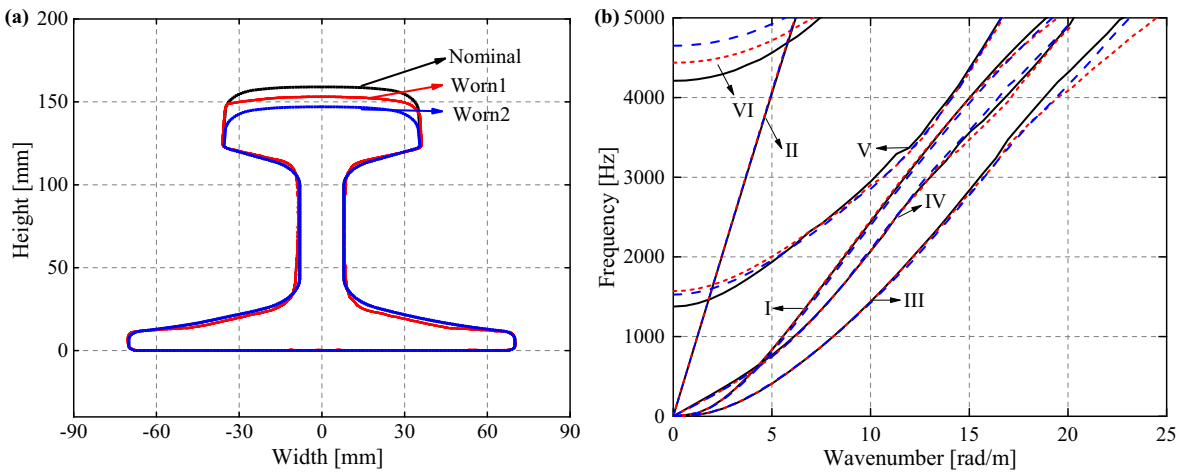


**Fig. A4.** Comparison of (a) rail heights: Nominal (—), Worn 1 (—), Worn 2 (—) (b) their wavenumber-frequency curves: Nominal (—), Worn 1 (---), Worn 2 (---).

measurements. Longitudinal compression waves (II) are not influenced by different rail heights because of the absence of cross-section deformation below 5 kHz. Vertical bending waves (I) are not sensitive to rail heights because cross-section deformation of these waves mainly occurs in the rail foot, which is almost identical in the three cases. The small difference between them in the whole frequency range comes from the different vertical area moments of the cross-sections.

## References

- [1] D.J. Thompson, Railway Noise and Vibration: Mechanisms, Modelling and Means of Control, Elsevier, 2008.
- [2] K. Hempelmann, K. Knothe, An extended linear model for the prediction of short pitch corrugation, *Wear* 191 (1–2) (1996) 161–169.
- [3] H. Ilias, The influence of railpad stiffness on wheelset/track interaction and corrugation growth, *J. Sound Vib.* 227 (5) (1999) 935–948.
- [4] S. Li, Z. Li, A. Núñez, R. Dollevoet, New insights into the short pitch corrugation enigma based on 3D-FE coupled dynamic vehicle-track modeling of frictional rolling contact, *Appl. Sci.* 7 (8) (2017) 807.
- [5] S.L. Grassie, R.W. Gregory, D. Harrison, K.L. Johnson, The dynamic response of railway track to high frequency vertical excitation, *J. Mech. Eng. Sci.* 24 (2) (1982) 77–90.
- [6] P. Koziol, Experimental validation of wavelet based solution for dynamic response of railway track subjected to a moving train, *Mech. Syst. Sig. Process.* 79 (2016) 174–181.
- [7] L. Xu, W. Zhai, A three-dimensional model for train-track-bridge dynamic interactions with hypothesis of wheel-rail rigid contact, *Mech. Syst. Sig. Process.* 132 (2019) 471–489.
- [8] W. Scholl, Schwingungsuntersuchungen an Eisenbahnschienen, *Acta Acust. United Acust.* 52 (1) (1982) 10–15.
- [9] D.J. Thompson, Wheel-rail noise generation, part III: rail vibration, *J. Sound Vib.* 161 (3) (1993) 421–446.
- [10] T.X. Wu, D.J. Thompson, A double Timoshenko beam model for vertical vibration analysis of railway track at high frequencies, *J. Sound Vib.* 224 (2) (1999) 329–348.
- [11] K.L. Knothe, Z. Strzyzakowski, K. Willner, Rail vibrations in the high frequency range, *J. Sound Vib.* 169 (1) (1994) 111–123.
- [12] L. Gavrić, Computation of propagative waves in free rail using a finite element technique, *J. Sound Vib.* 185 (3) (1995) 531–543.
- [13] M. Oregui, Z. Li, R. Dollevoet, An investigation into the vertical dynamics of tracks with monoblock sleepers with a 3D finite-element model, *Proc. Inst. Mech. Eng. Part F J. Rail Rapid Transit* 230 (3) (2016) 891–908.
- [14] L. Xu, X. Chen, X. Li, X. He, Development of a railway wagon-track interaction model: case studies on excited tracks, *Mech. Syst. Sig. Process.* 100 (2018) 877–898.
- [15] R. Cettour-Janet, A. Barbarulo, F. Letourneau, G. Puel, An Arnoldi reduction strategy applied to the semi-analytical finite element method to model railway track vibrations, *Mech. Syst. Sig. Process.* 116 (2019) 997–1016.
- [16] T. Hayashi, W.J. Song, J.L. Rose, Guided wave dispersion curves for a bar with an arbitrary cross-section, a rod and rail example, *Ultrasonics* 41 (3) (2003) 175–183.
- [17] J. Ryue, D.J. Thompson, P.R. White, D.R. Thompson, Investigations of propagating wave types in railway tracks at high frequencies, *J. Sound Vib.* 315 (1–2) (2008) 157–175.
- [18] M. Sale, P. Rizzo, A. Marzani, Semi-analytical formulation for the guided waves-based reconstruction of elastic moduli, *Mech. Syst. Sig. Process.* 25 (6) (2011) 2241–2256.
- [19] I.I. Setschedi, P.W. Loveday, C.S. Long, D.N. Wilke, Estimation of rail properties using semi-analytical finite element models and guided wave ultrasound measurements, *Ultrasonics* 96 (2019) 240–252.
- [20] Otero, J., Galarza, N., Rubio, B., & Moreno, E. (2009). Semi-analytical finite elements methods for dispersion curves using higher order elements for long range ultrasonic testing. In 2009 IEEE International Ultrasonics Symposium (pp. 1966–1969). IEEE.
- [21] P.W. Loveday, C.S. Long, D.A. Ramatlo, Mode repulsion of ultrasonic guided waves in rails, *Ultrasonics* 84 (2018) 341–349.
- [22] R.M. Lin, T.Y. Ng, Frequency response functions and modal analysis of general nonviscously damped dynamic systems with and without repeated modes, *Mech. Syst. Sig. Process.* 120 (2019) 744–764.
- [23] D.J. Thompson, Experimental analysis of wave propagation in railway tracks, *J. Sound Vib.* 203 (5) (1997) 867–888.
- [24] M. Oregui, Z. Li, R. Dollevoet, Identification of characteristic frequencies of damaged railway tracks using field hammer test measurements, *Mech. Syst. Sig. Process.* 54 (2015) 224–242.
- [25] R.P.C. Sampaio, N.M.M. Maia, R.A.B. Almeida, A.P.V. Urueira, A simple damage detection indicator using operational deflection shapes, *Mech. Syst. Sig. Process.* 72 (2016) 629–641.
- [26] S.Y. Khoo, Z. Ismail, K.K. Kong, Z.C. Ong, S. Noroozi, W.T. Chong, A.G.A. Rahman, Impact force identification with pseudo-inverse method on a lightweight structure for under-determined, even-determined and over-determined cases, *Int. J. Impact Eng.* 63 (2014) 52–62.

- [27] C. Devriendt, G. Steenackers, G. De Sitter, P. Guillaume, From operating deflection shapes towards mode shapes using transmissibility measurements, *Mech. Syst. Sig. Process.* 24 (3) (2010) 665–677.
- [28] D. Gorjup, J. Slavič, M. Boltežar, Frequency domain triangulation for full-field 3D operating-deflection-shape identification, *Mech. Syst. Sig. Process.* 133 (2019) 106287.
- [29] H. Inoue, K. Kishimoto, T. Shibuya, Experimental wavelet analysis of flexural waves in beams, *Exp. Mech.* 36 (3) (1996) 212–217.
- [30] C.B. Xu, Z.B. Yang, X.F. Chen, S.H. Tian, Y. Xie, A guided wave dispersion compensation method based on compressed sensing, *Mech. Syst. Sig. Process.* 103 (2018) 89–104.
- [31] Y.Y. Kim, E.H. Kim, Effectiveness of the continuous wavelet transform in the analysis of some dispersive elastic waves, *J. Acoust. Soc. Am.* 110 (1) (2001) 86–94.
- [32] A. Katunin, H. Lopes, J.A. dos Santos, Identification of multiple damage using modal rotation obtained with shearography and undecimated wavelet transform, *Mech. Syst. Sig. Process.* 116 (2019) 725–740.
- [33] H. Jia, Z. Zhang, H. Liu, F. Dai, Y. Liu, J. Leng, An approach based on expectation-maximization algorithm for parameter estimation of Lamb wave signals, *Mech. Syst. Sig. Process.* 120 (2019) 341–355.
- [34] F.L. di Scalea, J. McNamara, Measuring high-frequency wave propagation in railroad tracks by joint time–frequency analysis, *J. Sound Vib.* 273 (2004) 637–651.
- [35] W. Sachse, Y.H. Pao, On the determination of phase and group velocities of dispersive waves in solids, *J. Appl. Phys.* 49 (8) (1978) 4320–4327.
- [37] B.J. Schwarz, M.H. Richardson, Introduction to operating deflection shapes, *CSI Reliabil. Week* 10 (1999) 121–126.
- [38] Avitabile, P. (2001). Experimental modal analysis. *Sound and vibration*, 35(1), 20-31.
- [39] M.V.J Kovacevic, Wavelets and subband coding, (1995). Vetterli, M., & Kovacevic, J. (1995). Wavelets and subband coding (No. BOOK). Prentice-hall.
- [40] A. Grinsted, J.C. Moore, S. Jevrejeva, Application of the cross wavelet transform and wavelet coherence to geophysical time series, *Nonl. Proc. in Geophys* 11 (561–566) (2004) 24.